PHYSICAL REVIEW D

PARTICLES AND FIELDS

THIRD SERIES, VOLUME 39, NUMBER 11 1 JUNE 1989

Search for the anomalous production of single photons in e^+e^- annihilation at $\sqrt{s}=29$ GeV

C. Hearty,* J. E. Rothberg, and K. K. Young
Department of Physics, University of Washington, Seattle, Washington 98195

A. S. Johnson, J. S. Whitaker, and R. J. Wilson
Department of Physics, Boston University, Boston, Massachusetts 02215

G. Bartha, D. L. Burke, P. Extermann,† P. H. Garbincius,‡ C. A. Hawkins, M. J. Jonker,§ L. Keller, C. Matteuzzi,§ N. A. Roe, and T. R. Steele
Stanford Linear Accelerator Center, Stanford University, Stanford, California 94309

R. J. Hollebeek
Department of Physics, University of Pennsylvania, Philadelphia, Pennsylvania 19104
(Received 14 September 1988)

This paper reports results of a search for production by radiative e^+e^- annihilation of particles that interact only weakly in matter. The search has been made in a data set corresponding to 110 pb^{-1} acquired with the ASP detector at the Stanford Linear Accelerator Center storage ring PEP ($\sqrt{s}=29$ GeV). No anomalous signal has been observed, which limits the number of generations of light neutrinos to be $N_\nu<7.9$ (at 90% C.L.). Limits are also placed on the masses of particles predicted to exist by models of supersymmetry.

I. INTRODUCTION

The ASP (anomalous single photon) experiment[1] was designed to search for the process

$$e^+e^-\rightarrow\gamma+\text{weakly interacting particles} \quad (1.1)$$

at the e^+e^- storage ring PEP ($\sqrt{s}=29$ GeV) at the Stanford Linear Accelerator Center (SLAC). The experimental signature for this process is a single photon observed in the final state, with transverse momentum that cannot be balanced by particles lost down the beam pipe. The purpose of this measurement is to obtain information about the production of particles that are difficult to observe directly in the laboratory. Because of the general nature of this reaction—the unobserved particles can be anything, as long as they interact only weakly—the results of this measurement can be used to constrain new particle production in different models. In particular, the results of this experiment have been interpreted in the framework of the standard model[2] to place limits on the number of light-neutrino flavors, and in the context of models of supersymmetry[3–5] to place limits on the masses of proposed new particles.

In this experiment, we found a significant signal which was consistent with that expected from known standard-model sources. In the following sections, we will discuss the physics involved, describe in some detail the ASP apparatus, followed by the analysis and results, and finally we will discuss the interpretation of these results and compare and combine them with results from other comparable experiments.

II. THE PHYSICS OF ANOMALOUS SINGLE-PHOTON PRODUCTION

A. Single photons from known physics

The known standard-model contribution to (1.1) is the radiative production of neutrino-antineutrino pairs: $e^+e^-\rightarrow\gamma\nu\bar{\nu}$. The lowest-order Feynman diagrams for this process are shown in Fig. 1. The cross section for N_ν generations of neutrinos, in the local-limit (or four-point) approximation, is[6]

$$\frac{d^2\sigma_{\gamma\nu\bar{\nu}}}{dx\,dy}=\frac{2\alpha}{\pi}\frac{(1-\frac{1}{2}x)^2+\frac{1}{4}x^2y^2}{x(1-y^2)}\sigma_{\nu\bar{\nu}}(s')\ , \tag{2.1}$$

$$\sigma_{\nu\bar{\nu}}(s')=\frac{G_F^2 s'}{12\pi}\left[\frac{N_\nu(g_V^2+g_A^2)+2(g_V+g_A)(1-s'/m_Z^2)}{(1-s'/m_Z^2)^2+\Gamma_Z^2/m_Z^2}+2\right]\ , \tag{2.2}$$

where $y=\cos\theta$ (θ is the polar angle of the detected photon), $x=2E/\sqrt{s}$ (E is the energy of the photon), $g_A=-\frac{1}{2}$, and $g_V=2\sin^2\theta_W-\frac{1}{2}$. $\sigma_{\nu\bar{\nu}}(s')$ is the total $\nu\bar{\nu}$ production cross section evaluated for the reduced center-of-mass energy: $s'=s(1-x)$. The cross section can be factored this way because of the local-limit approximation. This approximation is strictly valid only for $s\ll m_W^2$; however, (2.1) agrees very well with the full calculation[7] for PEP energies. The term in (2.2) proportional to N_ν arises from the neutral current [Fig. 1(a)], while the final term of 2 in large parentheses is due to charged-current production of the electron neutrino [Fig. 1(b)]. The remaining terms result from the interference between the charged- and neutral-current production of electron neutrinos. The total Z width is

$$\Gamma_Z=\frac{m_Z^3 G_F}{12\pi\sqrt{2}}(21+N_\nu-48\sin^2\theta_W+64\sin^4\theta_W)\ , \tag{2.3}$$

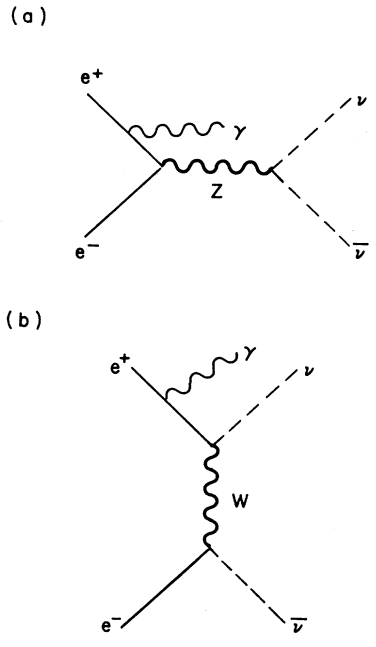

FIG. 1. Lowest-order contributions to (2.1). (a) The neutral-current contribution occurs for all types of neutrinos, while (b) the charged current produces electron neutrinos only. There is an additional charged-current diagram in which the photon is emitted from the W.

where the Z is assumed to decay into six quarks, three charged leptons, and N_ν neutrinos. This dependence on N_ν means that (2.1) is not a linear function of N_ν. However, the cross section (2.1) does not depend strongly on the Z width at PEP energies, so to a very good approximation, it varies linearly with N_ν (Fig. 2). Ma and Okada[8] were the first to note that this dependence on N_ν would permit a measurement of (1.1) to be interpreted as a measurement of (or a limit on) N_ν. This measurement (or limit) is very reliable because the experimental signature is clear, and because the cross section can be readily calculated. For three generations of neutrinos, the standard model predicts an integrated cross section of 0.04 pb in the acceptance of the ASP detector. If this were the only source of single-photon events, then ASP would expect a few events for an integrated luminosity of 100 pb^{-1}.

B. Possible new sources of single photons

New generations of neutrinos would imply larger cross sections in accordance with (1.1). The radiative production of any weakly interacting particles other than neutrinos would be an additional contribution to (1.1). In the local-limit approximation (mass^2 of particle $\ll s\ll$ mass^2 of t-channel propagator), the radiative cross section is related to the total nonradiative cross section by[9]

$$\frac{d^2\sigma_\gamma}{dx\,dy}=\frac{2\alpha}{\pi}\frac{(1-\frac{1}{2}x)^2+\frac{1}{4}x^2y^2}{x(1-y^2)}\sigma_0(s')\ , \tag{2.4}$$

where $\sigma_0(s')$ is the total nonradiative cross section evaluated at the reduced center-of-mass energy. Note that Eq. (2.1) is of this form. A consequence of this relationship is that all processes give approximately the same angular

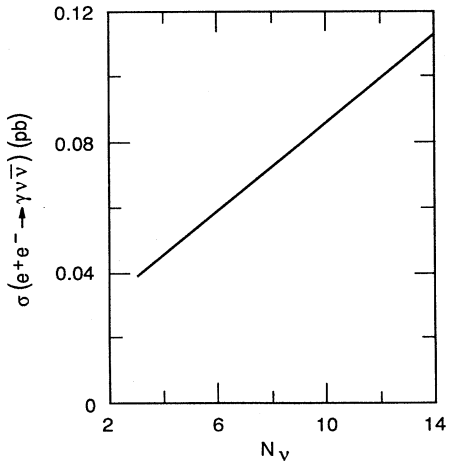

FIG. 2. Cross section for radiative neutrino production in the ASP acceptance region: $p_t>0.8$ GeV/c, $20°<\theta<160°$, and $E<10$ GeV.

and energy distributions for the observed photon. If the produced weakly interacting particles are massive, then the maximum photon energy is less than the beam energy. The detection of this end point—which would require a large number of events—would confirm the production of a massive particle. If the new particles were massless, it would be very difficult to separate the different contributions at a fixed center-of-mass energy. It may be possible, however, to distinguish them by performing this measurement at several different center-of-mass energies, as different contributions may have a different dependence on s.

Theories of supersymmetry (SUSY) predict the existence of particles that would contribute to the single-photon cross section. These theories propose that each known particle has a partner whose spin differs by $\frac{1}{2}$ unit but otherwise shares all conserved quantum numbers (such as charge or lepton number) except the new quantum number R (discussed below) that characterizes the supersymmetry. These superpartners share common interaction strengths so the cross section for the production of the SUSY particles is similar to that for the ordinary particle. The fact that none of these particles has been found indicates that if SUSY exists, it must be a broken symmetry—the SUSY particles must, in general, have higher masses than their ordinary partners.

The consequence of the higher masses for the SUSY particles is to suppress the cross sections. If the SUSY particles have masses of the order of the W boson, then the cross sections will be of the order of those for weak interactions.

Associated with supersymmetry is a multiplicatively conserved quantum number called R parity. Ordinary particles are assigned $R=+1$, whereas SUSY particles have $R=-1$. Thus, SUSY particles must always be created in pairs by e^+e^- annihilations. Another consequence of R-parity conservation is that the lightest SUSY particle (LSP) must be stable; it could not decay into normal particles without violating R-parity conservation. Cosmological arguments[10] and most SUSY models suggest that the LSP must be uncharged and color neutral. It is to this LSP that all other SUSY particles eventually decay.

In many models of supersymmetry, the common choice for the LSP is the photino ($\tilde{\gamma}$), which is a mass eigenstate $\tilde{\chi}_1^0$ as well as a weak eigenstate. Since it interacts electromagnetically, one might expect it to interact in the detector. In fact, photino interactions are very weak compared to those of the photon because of the mass of the scalar electron ($\tilde{e}$). For example, the cross section for $\tilde{\gamma}e^-\rightarrow\tilde{\gamma}e^-$, the process which would initiate a shower in the detector (shown in Fig. 3) is[3]

$$\sigma_{\tilde{\gamma}e^-}=\frac{8\pi\alpha^2}{3}\frac{s}{m_{\tilde{e}}^4}\ . \tag{2.5}$$

The ratio of this to the similar neutrino interaction, $\bar{\nu}_\mu e^-\rightarrow\bar{\nu}_\mu e^-$, is

$$\frac{\sigma_{\tilde{\gamma}}}{\sigma_\nu}\approx\left[\frac{100\ \text{GeV}/c^2}{m_{\tilde{e}}}\right]^4 . \tag{2.6}$$

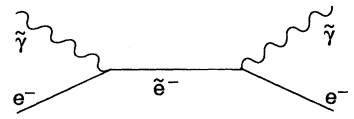

FIG. 3. Compton-type scattering of a photino.

At PEP and the DESY storage ring PETRA, a lower limit of 22 GeV/c^2 has been set on the scalar-electron mass by the absence of an anomalous rate of acoplanar electrons with missing energy produced in e^+e^- annihilations.[11,12] Thus, photino interactions are comparable in strength to neutrino interactions, and the radiative production of photino pairs (Fig. 4) could be a contribution to (1.1). There are two different scalar electron mass eigenstates that can contribute to (1.1) (due to the existence of left- and right-handed electrons). In general, SUSY models do not make firm predictions for the relative masses of these two eigenstates, so in this paper we quote results based on two extreme hypotheses: namely, that they are either degenerate or that one is much more massive than the other. The evaluation of these diagrams in the local-limit approximation in which it is assumed that ($m_{\tilde{\gamma}}^2 \ll s \ll m_{\tilde{e}}^2$) gives a cross section of the form (2.4), where σ_0, for the degenerate case is[4]

$$\sigma_0=\sigma_{\tilde{\gamma}\tilde{\gamma}}=\frac{2\pi\alpha^2}{3}\frac{s'}{m_{\tilde{e}}^4}(1-4m_{\tilde{\gamma}}^2/s')^{3/2}\ . \tag{2.7}$$

The only unknown parameters in this cross section are the photino and scalar-electron masses, so a measurement of the single-photon rate can be interpreted as a limit on these masses. The full calculation[13] to order α^3, rather than the local-limit approximation, was used to extract the mass limits from the data. The radiative-photino-pair-production cross section is plotted as a function of scalar-electron mass in Fig. 5. For scalar-electron masses less than 60 GeV/c^2, ASP would expect to observe a

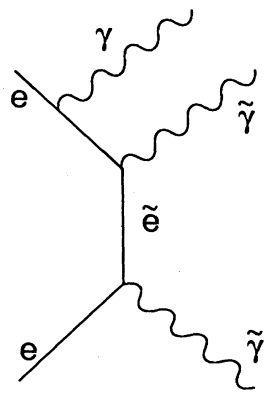

FIG. 4. Feynman diagram for the radiative production of photinos. The scalar-electron propagator can be either of two mass eigenstates. The photon can also be emitted by the scalar-electron propagator.

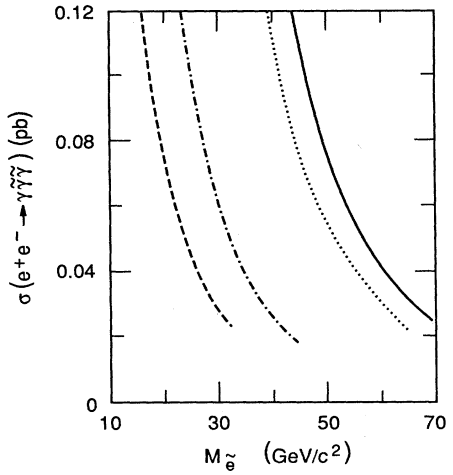

FIG. 5. The radiative photino cross section as a function of scalar-electron mass, for $m_{\tilde{\gamma}}=0$ (solid), $m_{\tilde{\gamma}}=6$ GeV (dotted), $m_{\tilde{\gamma}}=11$ GeV (dashed-dotted), and $m_{\tilde{\gamma}}=12$ GeV (dashed). The calculation assumes degenerate scalar-electron mass eigenstates; the cross sections are a factor of 2 lower if one is much heavier than the other.

significant increase in the cross section. Possible production of W-inos and other types of SUSY particles are discussed in the Appendix. All of these contribute to the single-photon cross section with a magnitude that is similar to the photino production cross section.

C. Background sources

An ideal hermetic detector that uniquely identified single photons emitted from the interaction point would eliminate all backgrounds. However, a practical detector for colliding beams must allow gaps for the beams. The ASP experiment is constructed such that it is completely hermetic except for gaps of less than 21 mrad along the beam lines. A gap in the experimental apparatus could potentially allow background events to simulate a signal as there may be events that produce a single photon into the apparatus and other particles into the gaps. Other sources may be characterized by a single photonlike signal accompanied by other low-energy debris that does not register in the apparatus. In the ASP experiment, we have minimized these effects by having no magnetic field and very little material between the interaction point and the sensitive parts of the detector.

Radiative Bhabha events are potentially the most serious background because of the high production cross section and the similarity to single-photon events—there actually is a photon that originates at the interaction point. Fortunately, these events can be rejected by a kinematic cut, as illustrated in Fig. 6. Since the ASP detector has no gaps above $\theta_{\text{veto}}=21$ mrad, both electrons must be below this angle if the event is to resemble a single photon. This restriction limits the projected transverse momentum of the photon (p_j is defined in Sec. III B)

$$p_j < 2\theta_{\text{veto}} E_{\text{beam}} = 0.6 \text{ GeV}/c \ . \tag{2.8}$$

Because of the finite resolution of the detector, the p_j

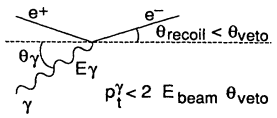

FIG. 6. Kinematics used to eliminate radiative Bhabha and other QED events.

threshold was set somewhat higher. To determine this threshold, we calculated[14] the distribution of these radiative Bhabha events and folded in the resolution and analysis efficiency of this experiment. Figure 7 shows the negligible contribution of these events within the fiducial region.

A second potential source of QED background arises from $e^+e^- \to \gamma\gamma$ events in which one of the photons fails to convert in the lead glass. The result is a single beam-energy photon in the detector. These events are eliminated by restricting the search to photons with energy less than 10 GeV. This cut hardly affects the acceptance for the single-photon events because of the concentration of these events at low p_j.

Another source of beam-related events comes from collisions between the beam particles and the residual gas in the beam line. Beam-gas events that produce a π^0 may simulate the signal (Fig. 8); the π^0 decays into photons that propagate into the apparatus, while the other final-state products stay in the beam line or are absorbed by the beam line components. These events are mostly eliminated by the detection of the small amounts of debris left in the detector away from the photons and by the characteristic energy deposition of the two photons resulting from the π^0 decay. We make a final test of these events in the final sample by examining the spatial distribution of the signal; beam-gas events have a line rather than a

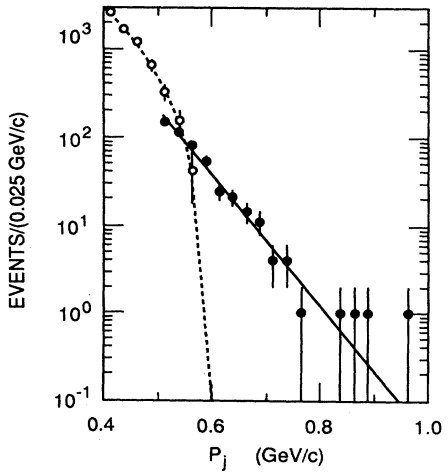

FIG. 7. Projected p_t distribution of photons in radiative Bhabha events before detector resolution and efficiency is applied (dashed line, open circles) and after (solid, closed circles). The points represent a Monte Carlo prediction of the number of events expected to be observed for 34 times the actual integrated luminosity.

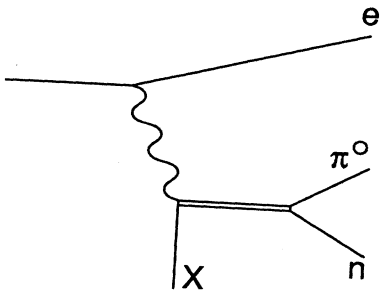

FIG. 8. Photoproduction of a neutron and a π^0. The neutron is not detected, while the π^0 can be mistaken for a photon.

point source.

While most cosmic rays entering the apparatus are characterized by penetrating minimum ionizing tracks, a small fraction of the cosmic rays are highly ionizing and could mimic single-photon events. The first level of elimination of the cosmic rays was to shield the detector from all but muons by locating the experiment at a depth of 20 m. The remaining cosmic rays that trigger the detector are removed by time-of-flight requirements and pattern recognition in the detector.

The above cuts are sufficient to suppress these backgrounds to the levels required in the ASP experiment for photons in the fiducial region:

$$p_t > 0.8 \text{ GeV}/c, \quad E \leq 10 \text{ GeV}, \quad 20° < \theta < 160° .$$

III. THE APPARATUS

A. Overview

The ASP detector was specifically designed for the search for single-photon final states. Important features were a large acceptance for photons and the ability to veto particles at very small angles (Figs. 9 and 10). The data were taken during several running periods. The

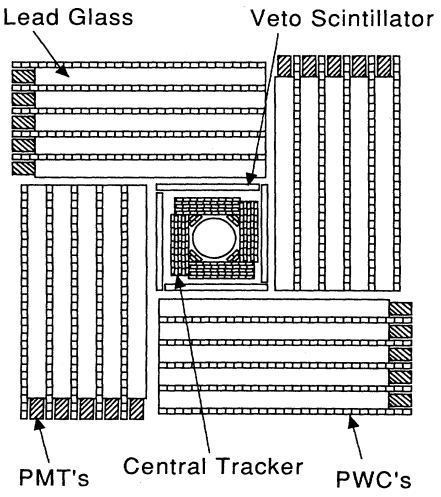

FIG. 9. Cross-section (XY) view of the central region of the ASP detector.

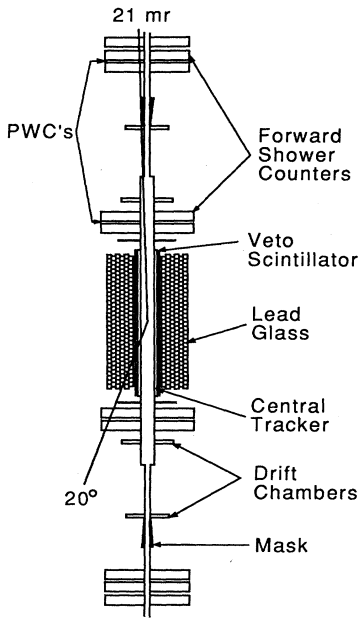

FIG. 10. A horizontal cross section (XZ) of the ASP detector. The apparatus is 8.8 m long and 1.2 m wide. The $\theta_p = 20°$ line marks the minimum angle for photon recognition. The $\theta = 21$ mrad line is the angle above which ASP has complete tracking and calorimetric coverage.

ASP detector was located in region 10 of the PEP e^+e^- collider at SLAC. PEP had center-of-mass energy $\sqrt{s} = 29$ GeV and a typical luminosity of 3×10^{31} cm^{-2}sec^{-1}.

This experiment was the first experiment designed specifically to look for single-photon final states. The ASP detector had three primary advantages over larger, general-purpose detectors. First, it had nearly complete solid-angle coverage; the only gaps were within 21 mrad of the beam direction. This permitted us to search for photons with a lower transverse momentum than other detectors, and to be certain that there were not other unobserved particles in the final state. The second advantage was good calorimeter segmentation, and nontower geometry which permitted good photon identification and a three-dimensional reconstruction of the photon momentum vector, including the origin of the photon along the beam line. The third advantage was the absence of a magnetic field, which permitted the detection of low-energy particles that originated from the beam line. These features were essential for the required level of background suppression. The good veto capability resided in the forward region of the detector, which is described in Sec. III D, while the central region—discussed in Sec. III C—provided photon measurement, charged particle veto, and detection of background debris. The detector was also optimized to record Bhabha and radiative Bhabha events that were essential to the calibration and normalization of the experiment.

The detector was monitored for stability and efficiency throughout the data-taking period. All subsystems were calibrated every few hours and a small fraction of the data was analyzed in real time to verify the detector

response. Various classes of events that were useful for diagnostic purposes and for off-line recalibration of the detector were recorded using specific triggers. These events included Bhabha ($e^+e^-\to e^+e^-$) and radiative Bhabha ($e^+e^-\to\gamma e^+e^-$) events, cosmic rays, and random beam crossings. The radiative Bhabha events were especially useful because they provided topologies that were used to calibrate the hardware as well as to evaluate and calibrate the software algorithms used for all parts of the experiment. The Bhabha events were used to establish the luminosity of the PEP collider and the integrated luminosity of the ASP experiment.

B. The coordinate system

Since we will be referring to projections of vectors in the text, we will describe the coordinate system that we use. We use a right-handed coordinate system centered on the interaction point (IP). The positive X axis is horizontal, towards the center of the PEP ring, while positive Y is vertical and upwards. The Z axis is defined by X and Y to lie along the beam line; electrons move towards $-Z$. θ and ϕ have their normal definitions; θ is the angle between a line from the origin and the Z axis, while ϕ is measured in the XY plane counterclockwise from the X axis. The angular position of a shower in the detector is usually defined in terms of ϕ and projected θ (θ_p), rather than ϕ and θ. Projected θ is the angle between the Z axis and a line measured in the XZ or YZ planes. The relationship between θ and θ_p is

$$\tan\theta_p=(\tan\theta)\max(|\cos\phi|,|\sin\phi|)\ . \tag{3.1}$$

Projected θ is the natural coordinate for this detector because the lead-glass array measures projected θ. The central proportional wire chambers measure ϕ, so these two subsystems together determine the angular position of a track. The transverse momentum corresponding to θ_p is projected transverse momentum, defined by $p_j=E\sin\theta_p$. Ordinary transverse momentum is defined by $p_t=E\sin\theta$, so $p_j\le p_t$. To be precise,

$$p_j=\frac{p_t}{\sqrt{\sin^2\theta+\sec^2\phi\cos^2\theta}}\ . \tag{3.2}$$

Therefore, $p_j=p_t$ for $\phi=0°$, 90°, 180°, and 270°.

The origin of a shower is specified by two quantities, R and R_{xy}. R is the signed distance of closest approach to the IP of a shower projected onto the XZ or YZ planes. It is defined by $R=Z\sin\theta_p$, where Z is the intercept of a shower with the Z axis in the XZ or YZ planes. R_{xy} is the distance of closest approach of the shower to the beam line or, equivalently, the distance of closest approach to the IP of a shower projected onto the XY plane.

C. The central detector

The central detector comprised several subsystems each with complete azimuthal coverage and polar-angle coverage from 20 to 160°. The central detector provided the capability for measuring the four-momentum of electrons and photons, and for distinguishing photons from electrons. An array of proportional tubes with three-dimensional readout, the central tracker (CT), filled the innermost region around the beam pipe. The CT was enclosed by a segmented scintillation counter with coarse spatial readout. These charged-particle detectors were in turn surrounded by a segmented lead-glass electromagnetic calorimeter. An array of time-of-flight scintillation counters formed an umbrella over the detector and was used to identify cosmic rays.

The amount of material in the beam pipe and flanges was kept to a minimum. At polar angles above 21 mrad, the thickness was about 0.03 radiation lengths; a flange between 30 and 44 mrad was the only significant additional material.

Lead-glass calorimeter.[15] The photon energies and momenta were measured with an array of 632 extruded F2- (Schott-) type lead-glass bars interleaved with proportional wire chambers (PWC's). With this system, we could identify photon signals and reconstruct the electromagnetic showers. Each lead-glass bar was $6\times6\times75$ cm with the long dimension transverse to the beam. They were arranged in four quadrants five layers deep so as to leave no gaps in the calorimeter between quadrants. A half-block offset between layers ensured that the small gaps between bars did not line up with the IP, and thereby improved the photon vertex resolution along the beam axis. The Čerenkov light was collected by a photomultiplier tube on each bar.

Lead glass was used because of its good intrinsic resolution and its stability. The lead glass was doped with 0.35% Ce to reduce its sensitivity to radiation damage. As further protection, the lead-glass array was designed to separate into two L-shaped halves that were retracted behind lead walls during beam injection. These steps to protect the lead glass from radiation damage were successful as the response of the glass remained unchanged throughout the running period. The calibration of the lead glass was monitored by means of a light fiber attached to each bar. A single light-emitting diode (LED), which could be pulsed at four different levels using filters, supplied light to all of the fibers in a quadrant. An extra reference tube in each quadrant compared the LED light with the light from a Na-I americium source to monitor the stability of the LED.

Cosmic rays were used to find correction factors that were applied off line to reduce the tube-to-tube gain variation to less than 2% and as a final check on the time variation of the response of the system. The absolute energy calibration as a function of θ and ϕ was carried out using kinematically fitted radiative Bhabha events. A lookup table was constructed and used to correct for variation in the Čerenkov light-collection efficiency as a function of position and angle, and for leakage of the shower from the lead glass.

The energy resolution of the lead-glass counters (for this analysis), averaged over all values of ϕ and projected θ in the region $20°<\theta_p<160°$, was $\sigma_E/E=14\%/\sqrt{E}$ (E in GeV) for an approximately 1-GeV shower.[16] The resolution was slightly poorer for showers entering the lead glass at quadrant boundaries.

The angular resolution was measured to be $\sigma_{\theta_p}=4.4°$, and the event time (event occurrence relative to the beam crossing time) was determined with a σ_T that ranged from 1.2 ns for a 1-GeV shower to 1.0 ns above 2.5 GeV. The ability of the detector to establish the origin of showers was characterized by its resolution in R, $\sigma_R=2.8$ cm. These resolutions, and those of the central PWC, were measured with the fully reconstructed and kinematically fitted radiative Bhabha events. (See Fig. 11.)

Between the layers of lead glass were planes of shower sampling PWC's that measured the azimuthal angle ϕ with a resolution of $\sigma_\phi=3.2°$, and permitted us to extract the distance of closest approach of the shower to the beam line, R_{xy}, with resolution $\sigma_{xy}=5.5$ cm.

Central tracker. The innermost of the charged-particle detectors was the "central tracker" (CT) which surrounded the beam pipe. The CT consisted of 192 thin-walled (wall thickness 0.3 mm) proportional wire tubes of dimension $2.4\times1.1\times220$ cm. There were five layers in four quadrants of 48 tubes each, arranged so as to ensure that all tracks passed through at least five tubes. The tubes were read out at both ends, so that charge division could be used to measure the Z position of charged particles. The veto efficiency, defined as the fraction of charged particles tracked by the CT, was measured to be 99.6% using cosmic rays that were selected to pass near the interaction point. During running conditions, the resolution in Z was approximately 3.3 cm or 1.5% of the wire length.[17]

Veto scintillator. The veto scintillator surrounding the central tracker was constructed from 1-cm-thick sheets of Kiowa scintillator. A double thickness of such sheets, of dimension 33.5×225 cm, surrounded the beam pipe in the central region at a distance of 16 cm from the beam line. The scintillator was read out with a wavebar and a photomultiplier tube at each end, permitting a determination of the Z position of the shower with an accuracy of $\sigma_Z=15$ cm. Two additional scintillation counters of dimension $2\times32\times60$ cm immediately in front of each inner forward shower counter (FSC) provided additional veto capability in the forward region.

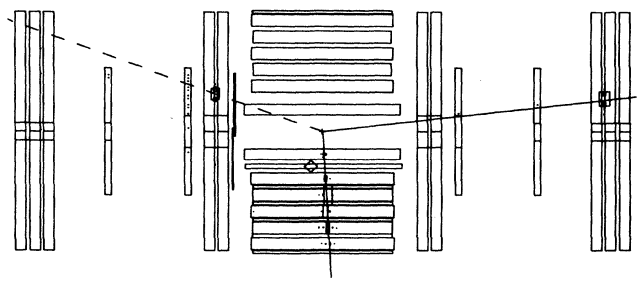

FIG. 11. A radiative Bhabha event in a horizontal cross section (XZ) of the ASP detector. The size of the box drawn for a lead-glass bar is proportional to the energy detected in that bar. The vertical scale is expanded by a factor of 3. The cross in the central tracker marks the centroid of the track found by the CT.

Time-of-flight system. The central region was covered by an array of 48 scintillator counters, of dimension $2.5\times20\times345$ cm oriented parallel to the beam line. This scintillator array was installed above the central detector. Each counter had a photomultiplier tube at each end; the Z position of the shower could be measured with a resolution of $\sigma_Z=26$ cm (7.5% of the counter length). The timing resolution, after compensating for flight time from the IP, was $\sigma_T=3$ ns. This system was used primarily to reject cosmic-ray events.

D. The small-angle detectors

The forward detectors consisted of electromagnetic calorimeters (FSC's) and tracking drift chambers. These detectors combined to give good tracking with good energy resolution for high-energy electrons over the complete azimuth in the polar-angle regions from 21 mrad to 20°.

The FSC's were constructed of lead-scintillator sandwiches with interleaved proportional wire chambers. These calorimeters were used as a veto against particles in the small-angle region and also as the luminosity monitors for the experiment. The FSC's were built in six radiation length modules of dimension 1.2 m square. A module consisted of layers of lead (0.6 cm Pb) alternated with 1.3-cm layers of Polycast PS-10 acrylic scintillator. Each edge of the module was covered by a sheet of Rohaglas GS1919 wavelength shifter and was read out with an Amperex XP2212PC phototube. There were two such modules at $|Z|=1.5$ m (the inner FSC's) and three at $|Z|=4.1$ m (the outer FSC's). Each module was built in two halves so that it could be easily installed around the beam pipe, but had a 4 cm overlap between the halves, giving complete coverage above 21 mrad.

The resolution of the FSC's was measured using Bhabha events to be $\sigma_E/E=25\%/\sqrt{E}$ (E in GeV) at 14.5 GeV. The FSC's received radiation doses of 100 000–500 000 rads in the course of the experiment. Phototube high voltages were periodically adjusted to compensate for the reduction in scintillator light output due to radiation damage. After several months of running, the FSC's were opened and the scintillators were exposed to infrared light. This annealing restored the scintillator to nearly its original light output.

Behind the first module of the FSC's in each region were two planes of proportional wire chambers, one plane oriented along each of the X and Y directions. There were 48 chambers per plane (six sets of eight chambers), each chamber measured $1.23\times2.36\times120$ cm in size. The angular resolutions were $\sigma_\theta=2.5$ and 28 mrad.

Charged particles in the forward region were tracked by four planes of drift chambers located between the inner and outer FSC's. These measured X and Y with a resolution of $\sigma=0.4$ mm at $|Z|=1.9$ and 3.0 m. The tracking capability was not used to select single-photon events, but was used to kinematically fit radiative Bhabha events.

In addition to the active elements discussed above, a tungsten mask was placed in an indentation in the beam pipe. This mask, which covered the region $12<\theta<21$ mrad, defined the minimum angle acceptance of the

FSC's, and protected the central region of the beam pipe from off-energy, off-angle electrons that would have grazed the beam pipe. These grazing electrons could have generated background single-photon events.

IV. TRIGGERING AND MONITORING

A. Trigger

The trigger decision was made on the basis of analog sums of lead-glass, scintillator, and FSC signals.[18] This decision was available less than 1 μs after the beam crossing. The time between beam crossings was ≈ 2.5 μs, so that no dead time resulted from the trigger decision. When the trigger conditions were satisfied the analog data from all subsystems were digitized in about 10 ms by a BADC/SHAM IV (Ref. 19) system and were recorded by a VAX 11/750 computer system.

The detector was monitored, on line, by analyzing a few percent of the data as they were recorded. Quantities characterizing the performance, such as resolutions and efficiencies, were calculated for each subsystem and compared with expected values. These higher-level checks complemented the individual subsystem calibration procedures to assure that the apparatus was working with high efficiency at all times.

The physics triggers selected events that were consistent with being single photons, radiative Bhabha events, or Bhabha events, as well as any event with significant energy. The trigger designed specifically for the single-photon search required at least 0.7 GeV of energy in one quadrant or two adjacent quadrants, with at least 0.20 GeV in the second through fifth layers, and either less than 1 GeV or greater than 7 GeV in the FSC. The layer requirement was intended to exclude a known class of beam-gas events that deposited their energy almost entirely in the first layer. The energy distribution of events collected by this trigger is shown in Fig. 12 along with the distribution from the "total energy" trigger, which required greater than 1.6 GeV of energy in the lead glass. The plots demonstrate how the additional pattern requirements of the single-photon trigger permitted a lower-energy threshold. Events satisfying either trigger condition were used in the single-photon analysis.

Special monitoring triggers allowed us to record random beam crossings, cosmic rays, and Bhabha and radiative Bhabha events. The random events were used to determine occupancies of the detector subsystems. The cosmic-ray trigger required a coincidence between two central scintillators during a gate 15 ns before beam crossings. The minimum-ionizing tracks from these events were used in finding variations in lead-glass response from bar to bar, and in calculating the central-tracker efficiency. The Bhabha trigger, which required high-energy particles in the forward regions, provided events used to determine the integrated luminosity. The radiative Bhabha trigger required a high-energy particle in at least one outer FSC and at least 0.2 GeV of energy in the lead glass.

The overall trigger rate was approximately 4.5 Hz. The rate from the single-photon trigger was ~ 2 Hz,

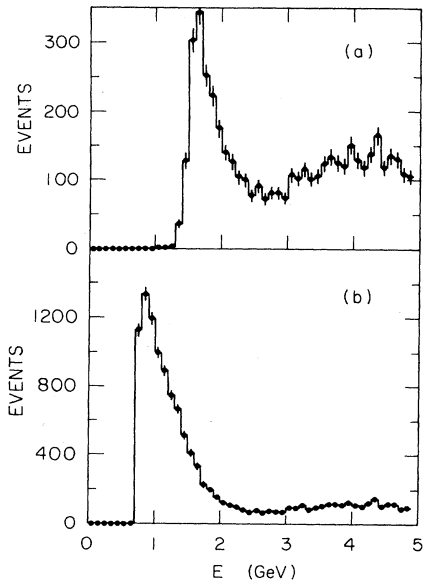

FIG. 12. Energy distribution of events recorded by the (a) "total energy" and (b) "single-photon" triggers.

while the rates for the other physics triggers and monitoring triggers were ~ 3 and ~ 1 Hz, respectively. These rates sum to more than the total rate because an event could satisfy the requirements of more than one trigger.

B. Monitoring with radiative Bhabha events

A subset of radiative Bhabha events was invaluable in the single-photon analysis because of similarity to single-photon events; the topology selected had an electromagnetic shower with no other energy in the central region of the detector, and two forward tracks. These events were useful in calibrating and monitoring the detector, developing analysis cuts, and determining the efficiency of the single-photon trigger and analysis.

The most common event topology, of which Fig. 11 is an example, had an electron in the central region, with an electron and a photon in the forward region (i.e., at polar angle small enough that the particle missed the lead glass). These fully reconstructed events were kinematically fitted using the measured energies and angles of the forward tracks and the angles of the central track as measured by the central tracker. The result of this fit was a prediction of the parameters of the shower in the lead glass. After a χ^2 cut on the kinematic fit, there were 40 000 events with a central track of $p_j > 0.8$ GeV/c. The values of these predicted parameters, and the sample of events passing the χ^2 cut, were unbiased by lead-glass resolutions or possible inefficiencies, since no lead glass or central PWC information was used in the fit. The lead-glass energy required by the radiative-Bhabha trigger was much lower than the single-photon trigger threshold. This event sample was therefore suitable for use in measuring resolutions and efficiencies, including the single-photon trigger efficiency.

The radiative-Bhabha sample was also used to calibrate the central-tracker measurement of Z. For this purpose,

the lead glass and central PWC's but not the central tracker were included in the kinematic fit.

C. Luminosity measurements

The forward-shower-counter system was the on-line luminosity monitor for PEP. Coincidences between pulses from the FSC's were converted into a specific luminosity.

The integrated luminosity was determined by comparing the measured and predicted rates of Bhabha events. One of the scattered particles was required to be within the angular region $55 < \theta < 95$ mrad while the other particle was restricted to $50 < \theta < 100$ mrad. The comparison, which is shown in Fig. 13 gives $(109.6 \pm 0.5 \pm 1.1)$ pb^{-1}. The first error is statistical, while the second is systematic. The primary sources of systematic error are uncertainties in the QED prediction and in our predictions of the effects of the beam-pipe flange in the $30 < \theta < 44$ mrad range.

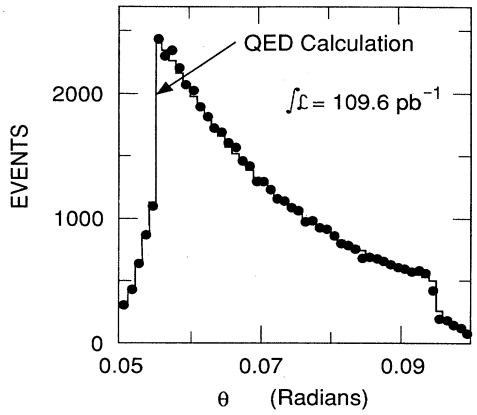

FIG. 13. Data and QED prediction for Bhabha scattering used to extract the integrated luminosity.

V. EVENT SELECTION

A. Overview

A total of 3×10^7 events were recorded on tape during data taking. This section describes the cuts that were used to reject all but 24 of these events. The majority of the events were rejected by vetoing on energy not deposited in a single shower and by photon shower requirements. A much smaller portion of the data required more sophisticated recognition algorithms that were developed by using our monitoring data. The efficiency of the event selection was measured using events recorded with diagnostic triggers. The cuts and their efficiencies are summarized in Table I.

The final 24 events were subjected to further analysis discussed in Sec. VI.

B. Finding events with spatially localized energy

We rejected multiparticle events by requiring that only that part of the detector containing the photon have any significant signal. To do this we divided the detector into several subsections for the purpose of occupancy cuts. These cuts rejected multiparticle events by requiring that only those subsections consistent with a single particle striking the detector show a significant signal. We rejected an event if any other subsections had more signal than a threshold or if any two other subsections had energy deposition exceeding a lower threshold. The thresholds were determined by observing the energy deposition of diagnostic events that were triggered at random during beam crossings. Figure 14 displays the fraction of these events that survived the threshold energy cut for the various subsections of the apparatus. These plots represent an average over all components of each subsystem for the full data set. The overall efficiency of this cut is 93%.

The next occupancy cut for those survivors of the above cuts required that the energy deposited in the last six radiation lengths (r.l.'s) of the inner FSC closest to the shower be less than 1 GeV. (This FSC was excluded from the threshold cut described in the preceding paragraph.) The energy deposited in the six r.l.'s closest to the lead glass was not included, because it depended upon the energy and angle of the shower. This cut was designed to eliminate a class of events in which a beam-gas interaction several meters from the IP could result in a high-energy particle striking the back of the inner FSC. The ensuing shower could leak through to the lead glass and appear to point back at the IP.

The final occupancy cut required that there be no central-tracker tracks. Note that this restriction not only eliminated events containing an extra charged particle, but also single charged-track events. These cuts were especially efficient for eliminating background because the absence of a magnetic field permitted even low-energy particles to register in our detectors. A photon that converted into an electron pair in the beam pipe would have been eliminated by this cut. The additional inefficiency due to random occupancy of the CT was measured using random beam crossings to be 5%, while the inefficiency due to early conversions of the photon and backsplash from the shower in the lead glass was calculated to be

TABLE I. Summary of event selection.

Cut	Events remaining	Reduction factor	Efficiency
Trigger (Sec. IV A)	30 000 000	1.0	1.0
Localized energy (Sec. V B)	64 000	470	0.83
Single particle (Sec. V C)	5 600	11.4	0.90
Cosmic ray (Sec. V D)	263	21.3	0.94
Shower shape (Sec. V E)	24	11.0	0.86
All cuts	24	1 300 000	0.61

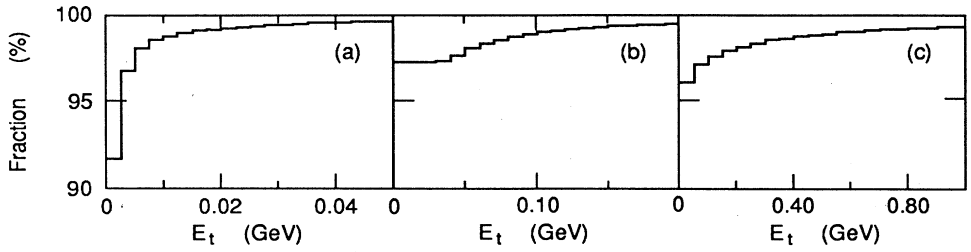

FIG. 14. Fraction of events (triggered at random during beam crossings) which survived the threshold energy cut E_t for (a) a lead-glass quadrant, (b) an inner and (c) an outer forward shower-counter region.

6.8%. The overall efficiency of the cuts described in this section was 83%. These cuts passed approximately 64 000 events of the 3×10^7 recorded triggers, representing a reduction by a factor of 470.

C. Reconstructing single-particle events

Many events that survived the localized-energy cuts were cosmic rays or beam-gas interactions. To further eliminate these types of events, we reconstructed the events to obtain the number of, the positions, the angles, and the energies of the particles. Only the events consistent with a single particle within the fiducial region were passed on to the next process. Most of the events that failed this cut were low-energy, beam-gas events.

If θ, ϕ, R, or R_{xy} could not be measured for the shower, or if the shower was not within the fiducial volume, the event was rejected. The measurement of θ and ϕ was required because the correction factors that convert the lead-glass signals into GeV are functions of these variables. A shower will have θ and R poorly measured if the photon does not convert early enough in the calorimeter; for this reason, only those showers that converted within the first five radiation lengths were used. If the shower was at a value of ϕ such that it passed between quadrants, then ϕ could be determined by both the central PWC's and the pattern formed by lead-glass layers with significant energy. This pattern of layers was required to be consistent with a shower originating from the beam—rather than a cosmic ray—and the value of ϕ determined by this pattern had to agree with the measurement of ϕ from the central PWC's. This last requirement helped to ensure that there was only one shower in the event.

A surviving event must have had a shower initiated by a neutral particle in the lead glass and no other significant energy in the detector. There are approximately 5600 events in the fiducial region that satisfied these criteria.

D. Eliminating cosmic-ray events

Cosmic-ray events which survived the earlier cuts were further reduced by tracking and timing cuts. The track was required to have $|R_{xy}|<3\sigma$ and event time, as measured by the lead glass, within $3\sigma_T$ of the beam-crossing time. If the event time had been determined by the time-of-flight system as well, this time must have been no earlier than 7 ns before the time found by the lead glass; i.e., the times were required to be consistent with a shower propagating away from the beam rather than toward it. Figure 15 shows that a good separation between cosmic rays and beam events can be obtained using these two event time measurements. These cosmic-ray cuts—especially the timing cuts—were an important aspect of this analysis. Although there were many more beam-gas background events than cosmic rays, the cosmic rays were not limited in p_j, and therefore were harder to distinguish from signal by the R-p_j likelihood analysis discussed later.

E. Determining the shower shape

The final set of cuts depended on the pattern of energy deposition in the lead glass and central PWC's. Two quantities were calculated for each lead-glass bar and PWC tube that contributed energy to the shower: W_i, the distance of closest approach of the central axis of the shower to the bar, and L_i, the distance to the bar along the shower. Two moments characterizing the shower shape were calculated from these quantities for both the lead glass and the PWC's, giving a total of four parameters that were used to identify photon showers:

$$M_{W2}=\frac{1}{E_{\rm sum}}\sum_i E_i W_i^2\ ,$$
$$M_{L1W2}=\frac{1}{E_{\rm sum}}\sum_i E_i W_i^2(L_i-\bar{L})\ , \tag{5.1}$$

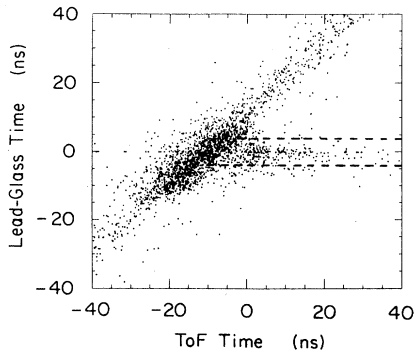

FIG. 15. Lead-glass time vs time-of-flight time. Cosmic rays fall into the diagonal band. The events retained by the timing cuts are designated by the dashed line.

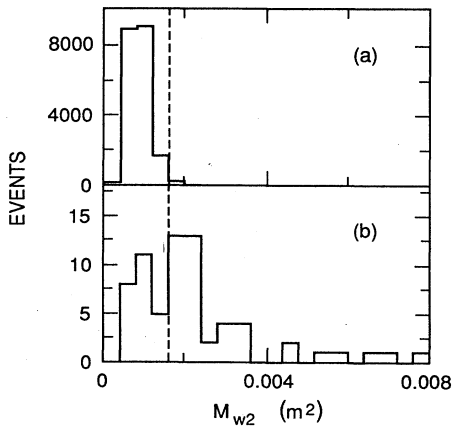

FIG. 16. Second-width-moment distributions measured by the lead glass for (a) radiative Bhabha events and (b) data. The cut (dashed line) retains events with $M_{W2} < 0.0016$ m^2. The events in these plots have passed all other cuts.

where the sum is over all bars or tubes above the noise threshold. E_i was the energy in a bar or tube, E_{sum} was the sum of the energy in these bars or tubes, and $\bar{L}$ was the average depth of the shower:

$$\bar{L} = \frac{1}{E_{\text{sum}}} \sum_i E_i L_i \ . \tag{5.2}$$

The M_{W2} cuts were designed to reject π^0's, which tend to form wider showers than photons. The M_{L1W2} cuts rejected events that showered too early or too late with respect to the centroid of the shower ($\bar{L}$). Note that the definition of M_{L1W2} made it independent of the conversion point of the photon and the point from which L_i is measured. We found that other moments defined from the quantities W_i and L_i were redundant. The distributions of M_{W2} in the lead glass for radiative Bhabha events and for single-photon candidates are compared in Fig. 16 to demonstrate the efficacy of the shower-shape cut. In both cases, the events have passed all other cuts.

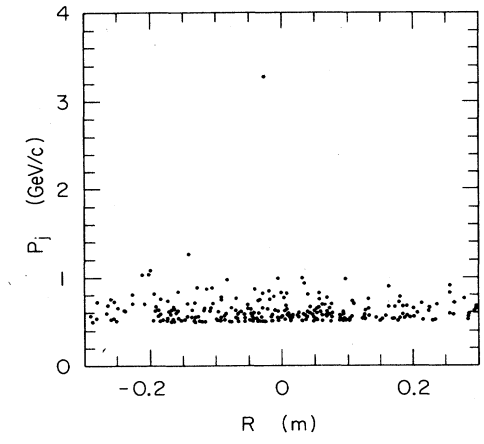

FIG. 17. R and p_j (projected-transverse-momentum) distribution of single-photon candidates with $p_j > 0.5$ GeV/c. Only the events with $p_j > 0.8$ GeV/c are used in the analysis. p_j is the transverse momentum of the shower measured in the XZ or YZ planes.

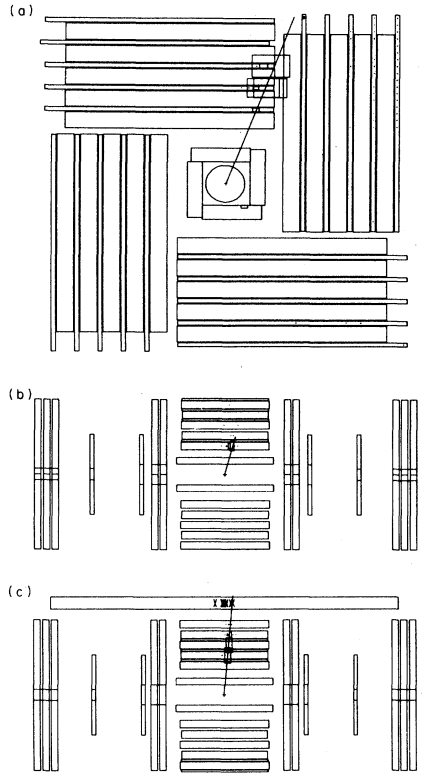

FIG. 18. (a) XY, (b) XZ, and (c) YZ views of the single-photon event which has $p_j = 3.2$ GeV/c.

The shower-shape cuts eliminated 239 of the remaining 263 events. The distribution of the remaining 24 single-photon candidate events in the variables R and p_j is shown in Fig. 17. The event with $p_j \approx 3.2$ GeV/c appears to be a real single-photon event, and is shown in Fig. 18.

VI. ANALYSIS OF THE FINAL SAMPLE

After the event-selection procedure described in the last section, we are left with 24 events with $p_j > 0.8$ GeV and $|R| < 0.3$ m. We have deliberately included background events with low p_j and large $|R|$ in this final sample so that we can perform a maximum-likelihood fit in these variables. Because the probability distributions for the signal and background events in R and p_j are very different, this method allows us to extract the most probable number of signal events. The signal is folded with the measured detection efficiencies and resolutions to calculate a production cross section.

A. Measurement of the detection and analysis efficiency

Inevitably, the selection procedure for eliminating backgrounds will have some inefficiency for true signal events. In this section, we describe our measurement of the efficiency for detecting single photons.

The efficiency for a single-photon generating process is given by the ratio of the number of events expected to be observed, given the resolution and the probability of a photon passing all cuts, to the number of events generated in the detector acceptance. Thus, the resolution of the detector must be considered in addition to the probability of an event passing all cuts. The resolution of the detector is folded with the probability of a photon passing the cuts by a Monte Carlo method. A Monte Carlo–generated event passes or fails the selection criteria as defined in a lookup table containing the probability to pass as a function of energy and position of the photon. If the event passes, new values for the energy and θ (representing the values measured by the detector) are selected from Gaussian distributions centered on the actual values. The ratio of the number of events passing in the fiducial region to the number generated in the region is the efficiency.

This procedure also determines the p_j distribution of photons created by the process being tested; it is the distribution of the events that pass. The p_j distribution of radiative Bhabha events is used to select the value of the p_j cut, while the distribution for radiative-neutrino events is used in the likelihood analysis of the final candidate events.

In order to find the probability of a photon passing all cuts, we applied all of the cuts outlined in Sec. V (with the exception of the 5 r.l. cut) to the radiative-Bhabha sample. The fraction that pass is stored in a lookup table as a function of the energy, θ and ϕ values obtained from the kinematic fit. The additional loss due to the 5 r.l. cut is calculated as a function of angle. This quantity and the occupancy-cut efficiency are included in this lookup table to give the overall probability of a single-photon event passing all cuts as a function of the photon's actual energy, θ and ϕ (Fig. 19). The dips in the efficiency versus ϕ plot result from the $20° < \theta_p < 160°$ requirement. A photon at $\theta = 20°$ will satisfy this requirement at $\phi = 0°$ but fail it at $\phi = 45°$ because of the square quadrant geometry. $e^+e^- \to \gamma\gamma$ events confirm the efficiency for high-energy photons passing the cuts presented in Sec. V.

The resolution of the detector is measured with those radiative Bhabha events that pass all cuts, and is recorded as a function of the kinematical-fit energy and angle. At low energies, the measured energy is biased towards higher values with respect to the actual energy. This bias represents the trigger efficiency of the detector: if the energy observed in the detector is a downwards fluctuation from the actual value, the event is less likely to satisfy a trigger requirement. The p_j resolution for a 2 GeV photon at $\theta_p = 30°$ ($p_j = 1.0$ GeV/c) is $\sigma = 0.15$ GeV/c.

The overall efficiency for detecting photons from radiative-neutrino production is 61% for $p_t > 0.8$ GeV/c, $E < 10$ GeV, and $20° < \theta < 160°$. All of the processes considered in this paper have similar photon spectra [Eq. (2.4)], so this efficiency is applicable for the SUSY analysis as well.

B. Finding the signal by maximum-likelihood analysis

To find the signal, we use a maximum-likelihood method applied to the hypothesis that we have a mixture of two distributions—the signal and the residual background. The data and the shape of the expected signal and background distributions in R and in p_j are shown in Figs. 17 and 20. This procedure optimizes our knowledge of the distributions and obviates the need to make explicit cuts in R and p_j, thus removing the need to calculate the efficiencies of these cuts or to perform a background subtraction.

This analysis assumes that the distributions of signal and background events in R and p_j are known, while the most probable amounts of signal ($\hat{S}$) and background ($\hat{B}$) are to be determined by the fit. These amplitudes—which are not required to be integers—are those values of S and B that maximize the generalized logarithmic likelihood function:[20]

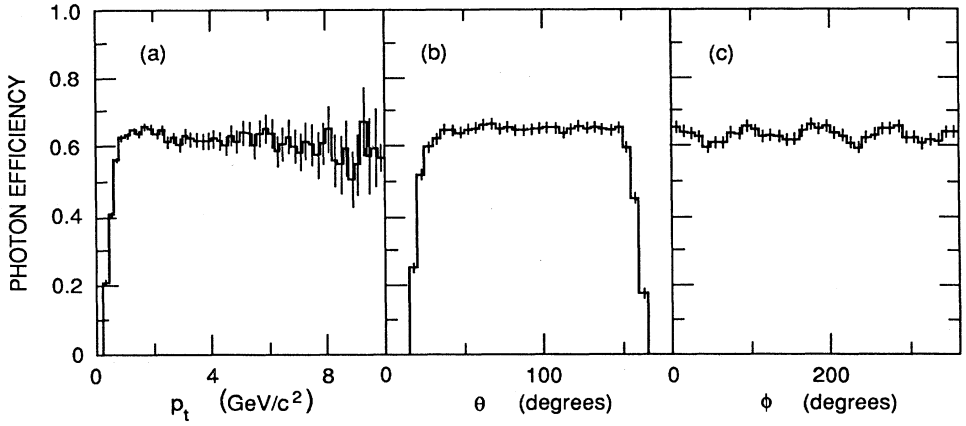

FIG. 19. The probability of a photon in a radiative neutrino event passing all cuts as a function of (a) p_t, (b) θ, and (c) ϕ. Plot (a) requires $20° < \theta < 160°$, while plot (b) requires $p_j > 0.8$ GeV/c. Plot (c) applies both restrictions.

$$\mathcal{L}(S,B)=\ln\left[\frac{e^{-(S+B)}(S+B)^N}{N!}\right]+\sum_{i=1}^{N}\ln\left[\frac{SP_S(R_i)P_S(p_j)+BP_B(R_i)P_B(p_j)}{S+B}\right]$$
$$=-(S+B)+\sum_{i=1}^{N}\ln[SP_S(R_i)P_S(p_j)+BP_B(R_i)P_B(p_j)]\ , \tag{6.1}$$

where $P_S(R)$, $P_S(p_j)$, $P_B(R)$, and $P_B(p_j)$ are the known distributions. An additional term of $-\ln N!$ is neglected in the last line as it does not depend upon S or B. The first term is the logarithm of a Poisson that ensures $\langle S+B\rangle=N$.

Beam-gas background and single-photon events have very different distributions in R and p_j (Fig. 20). As discussed in Sec. VI A, the signal p_j distribution was calculated from Eq. (2.4), folded with efficiency and resolution. The shape is well represented by a polynomial in the variable $\xi=1/\sqrt{p_j}$:

$$P_s(p_j)=\xi^3(a_0+a_1\xi+a_2\xi^2+a_3\xi^3+a_4\xi^4)\ , \tag{6.2}$$

where $a_0=-1.96$, $a_1=9.31$, $a_2=-11.44$, $a_3=6.20$, and $a_5=-1.38$. The signal R distribution was obtained from radiative Bhabha events that pass all cuts. It has the shape of a Gaussian with $\sigma=2.8$ cm, combined with an exponential tail of decay constant 8.1 cm that contains 3.3% of all events. The background p_j shape is an exponential of decay constant $\alpha=0.12$ GeV/c that is measured using events passing all cuts with $p_j>0.5$ GeV/c and $0.08<|R|<0.30$ m. The cut on R removed possible QED contamination. Finally, the background R distribution was found from events failing the shower-moments cuts but passing all other cuts. A parabola (parametrized as a second-order Legendre polynomial) was fitted to the R distribution of these background events:

$$P_B(R)=\frac{1}{2L}+\beta\left[\frac{3R^2}{L^2}-1\right]\ , \tag{6.3}$$

where $L=0.3$ m, and the fit gave $\beta=-0.48$.

The likelihood maximization gives $\hat{S}=1.6$ events with $p_j>0.8$ GeV/c.

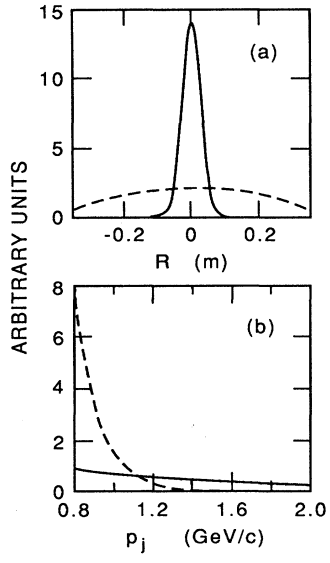

FIG. 20. Probability distributions for signal (solid) and background (dashed) in the variables (a) R and (b) p_j. The vertical scales are arbitrary but are the same for both signal and background.

VII. RESULTS

A. Limits on the production cross section and the number of neutrino generations

We use a Monte Carlo method to convert our measured quantities into a physics result. The physical quantity that we set a limit on is n_s—the mean number of single-photon events expected to be observed. That is,

$$n_s\equiv\sigma L\epsilon\ , \tag{7.1}$$

where σ is the total single-photon cross section from all sources, L is the total integrated luminosity, and ϵ is the overall efficiency. Thus, a limit on n_s is equivalent to a limit on the cross section. For various possible values of n_s we calculate the probability that an experiment equivalent to ASP would observe ≤ 1.6 events. The value of n_s for which this probability is 10% is interpreted as the 90%-C.L. upper limit on n_s. We find this probability by simulating many $R-p_j$ distributions for each value of n_s, since only this distribution is needed to perform the likelihood analysis. For each simulated equivalent experiment, the number of signal events generated is randomly selected from a Poisson distribution centered upon n_s. Values for R and p_j were randomly selected for each simulated signal event from the distributions $P_S(R)$ and $P_S(p_j)$. Similarly, the number of background events is selected from a Poisson distribution centered upon the number of background events actually observed, and values for R and p_j for each are selected from the distributions $P_B(R)$ and $P_B(p_j)$. This simulated R-p_j distribution is then analyzed using the maximum-likelihood method outlined in Sec. VI B, and the result compared to the 1.6 events actually observed. The 90%-C.L. limit is $n_s<4.8$, and the 95%-C.L. limit is $n_s<5.9$. This 90%-C.L. limit is equivalent to

$$\sigma(e^+e^-\to\gamma+\text{weakly interacting particles})<0.072\text{ pb} \tag{7.2}$$

in the fiducial region $p_t>0.8$ GeV/c, $E\leq 10$ GeV, $20^\circ<\theta<160^\circ$. This limit is valid for initial-state radiation

processes in which the final-state masses are less than a few GeV. The 95%-C.L. limit is $\sigma < 0.089$ pb. If single-photon events result from radiative-neutrino production only, these limits on the cross section are equivalent to

$$N_\nu < 7.9 \quad (90\%\ \text{C.L.})$$

and

$$N_\nu < 10.4 \quad (95\%\ \text{C.L.}) .$$

These limits are lower than those from any other single-photon searches.

B. Limits on the production of SUSY particles

The single-photon measurement can also be used to extract limits on the masses of SUSY particles. In this case, radiative-neutrino-antineutrino events constitute a background to this signal. Unlike the beam-gas background, which can be statistically separated from photons on the basis of the R and p_j distributions, neutrino events are identical to SUSY events. To set a limit on the presence of SUSY events, there are two general approaches.[21] The "classical" approach is to calculate the probability of making an observation, given a hypothesis about the physical parameter. The Bayesian analysis, on the other hand, finds the degree of belief that a physical parameter has a particular value, given that the observation was made. Numerically, the limits found are the same for many situations. Unfortunately, this is not the case here; limits obtained using both techniques are presented below. The Bayesian limits on SUSY masses are then compared to those from other e^+e^- experiments.

We employ a Monte Carlo simulation of many equivalent experiments in order to find the classical limits on the SUSY masses. The procedure is the same as that used to find the neutrino limits, except that the mean number of signal events is the number expected from three generations of neutrinos (2.6), plus the mean number of SUSY events expected to be observed ($n_{\rm SUSY}$). The p_j distributions are the same for these two types of events when the lightest SUSY particle (LSP) is massless. The 90%-C.L. upper limit on $n_{\rm SUSY}$, which is that value of $n_{\rm SUSY}$ for which 10% of simulated experiments obtain $\hat{S} < 1.6$, is $n_{\rm SUSY} < 2.2$. (The probability of observing $\hat{S} < 1.6$ when $n_{\rm SUSY} = 0$ is 33%.) Assuming that the photino is the LSP and is massless, and that the two scalar-electron mass states are degenerate, this limit is equivalent to $m_{\tilde{e}} > 64$ GeV/c^2. If three generations of massless scalar neutrinos are the LSP, then the corresponding limit in the W-ino mass is $m_{\tilde{W}} > 66$ GeV/c^2. We have summarized the classical lower limits for SUSY masses for 90% C.L. and 95% C.L. in Table II.

TABLE II. Classical lower limits set on SUSY masses by ASP in GeV/c^2.

	90% C.L.	95% C.L.
$m_{\tilde{e}}$(degenerate) ($m_{\tilde{\gamma}}=0$)	64	57
$m_{\tilde{e}}$(nondegenerate) ($m_{\tilde{\gamma}}=0$)	53	47
$m_{\tilde{W}}$ ($m_{\tilde{\nu}}=0$)	66	59

The classical limit on $n_{\rm SUSY}$ can be criticized because the simulated experiments include those in which more than 1.6 neutrino events are observed. The procedure is numerically equivalent to observing that the 90%-C.L. limit on 1.6 events is 4.8 events, subtracting 2.6 for the neutrino background, and obtaining the limit 2.2 events on $n_{\rm SUSY}$. This involves subtracting more neutrino background events than were actually observed. The Bayesian procedure[22,23] avoids this issue. The method is most easily understood in terms of the likelihood function for $n_{\rm SUSY}$, $\mathcal{L}(n_{\rm SUSY})$, which is proportional to the probability of observing 1.6 events when expecting $2.6+n_{\rm SUSY}$. [Thus, $\mathcal{L}(n_{\rm SUSY})$ has its maximum value at $n_{\rm SUSY}=0$.] For the purposes of this calculation, the number of events observed is assumed to lie in a Poisson distribution centered on $2.6+n_{\rm SUSY}$. Because of the beam-gas background, this is not strictly correct, but the error introduced by this assumption is small. The normalized likelihood function for $n_{\rm SUSY}$ is

$$\mathcal{L}(n_{\rm SUSY}) = \frac{(n_{\rm SUSY}+b)^N e^{-(n_{\rm SUSY}+b)}}{\int_0^\infty (s+b)^N e^{-(s+b)} ds} , \tag{7.3}$$

where $b=2.6$ and $N=1.6$. The 90%-C.L. upper limit on $n_{\rm SUSY}$ is l, where

$$\int_0^l \mathcal{L}(n_{\rm SUSY}) dn_{\rm SUSY} = 0.90 . \tag{7.4}$$

The disadvantage of the Bayesian procedure is that the resulting limits on physical parameters, such as particle masses, depend upon which variable is used to parametrize the likelihood function. For example, since we are endeavoring to obtain limits on $m_{\tilde{e}}$, we might be tempted to use $\mathcal{L}(m_{\tilde{e}})$. Unfortunately, $\mathcal{L}(m_{\tilde{e}})$ has its maximum value at $m_{\tilde{e}}=\infty$, and so cannot be normalized to satisfy $\int \mathcal{L}(m_{\tilde{e}}) dm_{\tilde{e}} = 1$. The justification in using $\mathcal{L}(n_{\rm SUSY})$ is that the limits obtained in the absence of background [i.e., $b=0$ in Eq. (7.3)] agree with those found using the classical procedure. Furthermore, since this parametrization has been used by the other e^+e^- single-photon searches, the limits can be directly compared. The 90%-C.L. and the 95%-C.L. upper limits are $n_{\rm SUSY} < 3.3$ and 4.2 events, respectively. These limits are equivalent to

$$\begin{aligned} &\sigma_{\rm SUSY} < 0.049 \text{ pb} \quad (90\%\ \text{C.L.}) , \\ &\sigma_{\rm SUSY} < 0.063 \text{ pb} \quad (95\%\ \text{C.L.}) , \end{aligned} \tag{7.5}$$

for the fiducial region defined earlier. The equivalent limits on the mass of the scalar electron, assuming that the photino is the LSP, are shown as a function of photino mass in Fig. 21. For a massless photino and degenerate scalar-electron mass states, the limit is

$$m_{\tilde{e}} > 57 \text{ GeV}/c^2 \quad (90\%\ \text{C.L.}) .$$

The mass limits for nondegenerate scalar-electron masses and for the 95%-C.L. mass limits are shown in Table III. The limits on the W-ino mass, obtained under the alternative hypothesis that the scalar neutrino is the LSP, and that there are three degenerate generations, are shown as

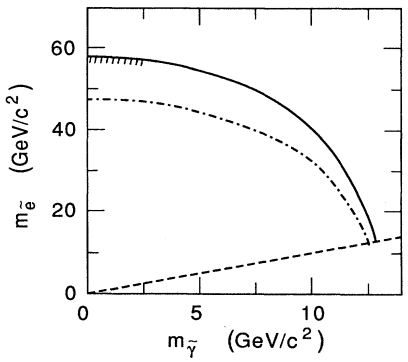

FIG. 21. 90%-C.L. limits placed on the scalar-electron and photino masses. The solid line applies if the scalar-electron mass states are degenerate, while the dashed-dotted line applies if one is much heavier than the other. The dashed line is $m_{\tilde{e}}=m_{\tilde{\gamma}}$.

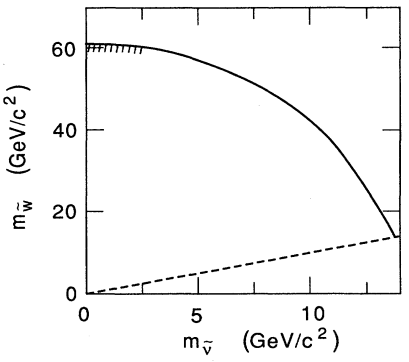

FIG. 22. 90%-C.L. limits placed on the W-ino and scalar-neutrino masses. The calculation assumes three degenerate scalar-neutrino generations. The dashed line is $m_{\tilde{W}}=m_{\tilde{\nu}}$.

a function of scalar-neutrino mass in Fig. 22. For massless scalar neutrino, the limit is

$$m_{\tilde{W}} > 59 \text{ GeV}/c^2 \quad (90\% \text{ C.L.}) .$$

These limits on the SUSY masses are significantly higher than those from other single-photon searches and are summarized in Table III. The limits in this table are either 90%-C.L. or 95%-C.L. Bayesian lower limits, and assume either a massless photino or a massless scalar neutrino.

C. Systematic errors

The primary systematic error on the neutrino limit arises from radiative corrections to Eq. (2.1). Although work has been done on these corrections,[24–27] the full α^4 calculation is not available. The inclusion of a second photon in the final state reduces the calculated cross section for two reasons: the second photon can veto the event, and the momentum carried by the second photon reduces the average transverse momentum of the primary photon, causing some events to fail the p_j cut. Reference 24 indicates that the loss is approximately 8% of the cross section due to Z^0 production. Such a loss could change our limit from $N_\nu < 7.9$ to $N_\nu < 8.5$. Another uncertainty in the cross-section calculation is the use of the local-limit approximation, which gives a cross section that may have an uncertainty of 4%. The effect of these uncertainties could be to increase the neutrino limit from 7.9 to 8.2. An incorrect Z^0 width used in Eq. (2.1) would lead to an incorrect cross section. However, as was mentioned in Sec. II A, the effect of the width of the Z^0 is negligible at the PEP energy, less than 0.1% of the cross section.

The other major source of error in the calculation of the cross section is a possible systematic bias in the measurement of p_j and θ_p, which would include events in the fiducial region that should be excluded, or vice versa. A related error, giving the same result, is the use of incorrect values for the resolution of the detector in these quantities. The size of these errors is estimated by applying the detector simulation to the four-vectors from the kinematic fit to radiative Bhabha events. (For this purpose, only those cuts that can be applied to radiative Bhabha events are simulated.) The number of simulated events within the fiducial region after this process can be directly compared with the actual number of radiative Bhabha events that are measured to be within the fiducial region and pass all cuts. This comparison indicates that the error in the calculated cross section from this source is less than 5%.

Two other sources of systematic error are the 1% uncertainty in the luminosity, and a 2% uncertainty that results from the use of electrons rather than photons to determine the single-photon efficiency. The limits obtained are not sensitive to small variations in the probability distribution functions used in Eq. (6.1). For example, changing the decay constant in $P_B(p_j)$ by 1σ results in a change of less than 0.5% in the limit given in Eq. (7.2).

TABLE III. Bayesian lower limits set on SUSY masses by ASP in GeV/c^2.

	90% C.L.	95% C.L.
$m_{\tilde{e}}$(degenerate) ($m_{\tilde{\gamma}}=0$)	57	53
$m_{\tilde{e}}$(nondegenerate) ($m_{\tilde{\gamma}}=0$)	47	43
$m_{\tilde{W}}$ ($m_{\tilde{\nu}}=0$)	59	56

VIII. DISCUSSION

A. The limit on the number of neutrino generations from single-photon experiments

The ASP experiment has completed the most sensitive search for the radiatively tagged production of particles that interact only weakly in matter—a search for which it was specifically designed. No anomalous signal has been observed. This absence has been interpreted as a limit on the number of generations of light neutrinos. At the 90% C.L., N_ν is restricted to be less than 7.9 generations.

The limits on the number of neutrino generations from the MAC (Ref. 28) and CELLO (Ref. 29) Collaborations

as well as the relevant parameters of each experiment are summarized in Table IV. We have combined these results with the ASP measurement to obtain a composite limit on N_ν. In combining the results a question arises as to whether to include the constraint $N_\nu \geq 3$. In the following discussion we give results both with and without this constraint.

The statistical method used to obtain the combined limits on N_ν from ASP, MAC, and CELLO is similar to the Bayesian analysis used to obtain the ASP limits on the masses of SUSY particles. We also use this method to extract the ASP limit on N_ν with the bound $N_\nu \geq 3$.

The parameter used in this analysis is n_s, the number of events expected to be observed; i.e., $n_s = \sigma \epsilon L$, where σ = radiative neutrino cross section, ϵ = overall analysis efficiency, and L = integrated luminosity. The normalized likelihood function for n_s for N observed events (not necessarily an integer) if no bound is placed on N_ν is

$$\mathcal{L}(n_s) = \frac{n_s^N e^{-n_s}}{\Gamma(N+1)} , \tag{8.1}$$

where $\Gamma(N+1)$ is a Γ function. $N = 3.86$ for the combination of the three experiments (Table IV). The 90%-C.L. upper limit on n_s is l, where

$$\int_0^l \mathcal{L}(n_s) dn_s = 0.90 . \tag{8.2}$$

From this equation we find $l = 7.8$ events.

A more conservative limit is found by requiring that $N_\nu \geq 3$. [Equation (8.2) could result in limits on N_ν less than three for some values of N.] The bound $N_\nu \geq 3$ is equivalent to requiring $n_s \geq b$, where b is the number of events expected for three neutrino generations (5.57 events for the three experiments). The normalized-likelihood function for n_s is then

$$\mathcal{L}'(n_s) = \frac{\mathcal{L}(n_s)}{\int_b^\infty \mathcal{L}(n) dn}, \quad n_s \geq b . \tag{8.3}$$

The 90%-C.L. limit on n_s with this likelihood function is

$$\int_b^l \mathcal{L}'(n_s) dn_s = 0.90 , \tag{8.4}$$

from which we find $l = 9.7$ events. Note that the upper limit found in this manner is always higher (less restrictive) than the unbounded case, regardless of the values of N and b.

Limits on n_s are converted to limits on N_ν by parametrizing n_s as a linear function of N_ν:

$$n_s = a + m N_\nu . \tag{8.5}$$

The parameters a and m are derived from the MAC (Ref. 28) and CELLO (Ref. 29) publications. The combined values for a and m are just the sums of those from the individual experiments.

The combined e^+e^- limits on N_ν, with and without the bound on N_ν, are

$$N_\nu < 5.2 \quad (N_\nu > 0) \tag{8.6}$$

and

$$N_\nu < 7.1 \quad (N_\nu \geq 3) . \tag{8.7}$$

The corresponding 95%-C.L. limits are $N_\nu < 6.4$ for $N_\nu > 0$, and $N_\nu < 8.1$ for $N_\nu \geq 3$. These 90%-C.L. limits are higher than those given by a similar analysis in Ref. 29. There are two reasons for this difference. The final analysis of the ASP experiment has reduced the systematic error in the determination of the luminosity, and has determined a lower integrated luminosity. This in turn has raised the ASP lower limit for N_ν compared to the earlier result used by Ref. 29. Also, Ref. 29 has used the unpublished limit for N_ν from the Mark J experiment, but we have chosen not to do so.

Equation (8.2) could be used to calculate limits for individual experiments, but both ASP and CELLO actually use Monte Carlo methods that explicitly include beam gas or cosmic-ray backgrounds. If ASP were to use (8.2), the 90%-C.L. limit would be $N_\nu < 7.8$, slightly better than the actual limit $N_\nu < 7.9$. The fact that these values agree well indicates that using (8.2) and (8.4) to find the combined limit is not unreasonable.

The ASP limit with the bound $N_\nu \geq 3$ is found from (8.4) with $N = 1.6$ and $b = 2.6$. The 90%-C.L. limit is $n_s < 5.9$ or $N_\nu < 10.4$.

TABLE IV. Summary of single-photon searches by e^+e^- experiments.

	ASP	MAC (Ref. 28)	CELLO (Ref. 29)	Combined
$\int L\,dt$ (pb^{-1})	110	177	123	
$\sqrt{s}$ (GeV)	29	29	35–42.6	
$p_t^{\min}$ (GeV/c)	0.8	2.0–4.5	1.75–2.3	
θ_{veto} (mrad)	21	66–175	50	
No. events expected	2.6	1.1	1.87	5.57
No. events observed	1.6	1.0	1.26	3.86
90% (95%) C.L. on n_s	4.8 (5.9)	3.9 (−)	3.9 (4.7)	7.8 (9.0)
Parameter a	1.27	0.49	0.83	2.59
Parameter m	0.44	0.20	0.35	0.99
90% (95%) C.L. on N_ν	7.9 (10.4)	17 (−)	8.7 (11.3)	5.2 (6.4)
90% (95%) C.L. on N_ν assuming $N_\nu \geq 3$	10.4 (12.3)		11.2 (13.9)	7.1 (8.1)

B. Comparison with results from proton-antiproton colliders

Experiments at the CERN $\bar{p}p$ collider also obtain limits on N_ν. The UA1 Collaboration uses a technique that is similar to the single-photon search; it is a search for the process $\bar{p}p \to Z^0 x$, followed by the decay $Z^0 \to \nu\bar{\nu}$ (Ref. 30). Although the Z^0 is not detected, the process can produce large missing transverse energy when there are one or more high-p_T (gluon) jets recoiling against the Z^0. In selecting possible candidate events, UA1 requires that the event have at least one jet with high transverse energy ($E_T > 12$ GeV), and have missing transverse energy that is significant to at least the 4σ level. The largest contribution to this sample is $W \to \tau\nu_\tau$ decays. Each event is assigned a likelihood of being such an event on the basis of the shower shape and particle content and those that are most likely (i.e., have a likelihood greater than 0) are assumed to be τ events and are not used in the subsequent analysis. Because of difficulties in the Monte Carlo simulation used, the additional restriction $E_T < 40$ GeV is applied, leaving 17 monojet events. The predicted rate of such events, assuming three generations of neutrinos, is $17.8 \pm 3.7 \pm 1.0$ events. The major contributions to this predicted rate are τ events that are not rejected by the likelihood cut, jet fluctuations (events that do not really have large missing transverse energy), and the desired neutrino events. For an expected rate of 1.8 events per extra neutrino generation, this measurement implies that $\Delta N_\nu < 7$ (90% C.L.), or

$$N_\nu < 10 \quad (90\%\ \text{C.L.}) .$$

A second method to measure N_ν, which is used by both UA1 and UA2 (Refs. 31 and 32), consists of measuring the ratio

$$R = \frac{\sigma(\bar{p}p \to Wx) B(W \to l\nu)}{\sigma(\bar{p}p \to Zx) B(Z \to l^+ l^-)} \equiv R_\sigma \frac{B_W}{B_Z} .$$

R_σ, B_W, and B_Z are calculated using the standard model and the measured nucleon structure functions. B_Z is a function of N_ν, so a measurement of R can be interpreted as a measurement of, or a limit on, N_ν. The calculation of B_W and B_Z depend on the top-quark mass, m_t. The results listed here are valid for $m_t > 44$ GeV/c^2 and assume that the charged leptons of any addition generations do not contribute to the W and Z decays. The current mass limit is $m_L > 41$ GeV/c^2 (Ref. 30) so such decays are still allowed experimentally. There is uncertainty in R_σ due to uncertainty in the nucleon structure functions but the major uncertainty in the measurement of N_ν is the statistical uncertainty from the small number of Z^0 leptonic decays. The limits obtained by these experiments are

$$N_\nu < 7.0 \quad (90\%\ \text{C.L.}) \quad \text{UA1} ,$$

$$N_\nu < 7.0 \quad (95\%\ \text{C.L.}) \quad \text{UA2} ,$$

$$N_\nu < 4.6 \quad (90\%\ \text{C.L.}) \quad \text{combined UA1 and UA2} .$$

If the additional requirement of $N_\nu \geq 3$ is applied, the combined limit is

$$N_\nu < 5.9 \quad (90\%\ \text{C.L.}) .$$

C. Results from astrophysics

In addition to the laboratory experiments discussed above, N_ν can be determined by astrophysics arguments and measurements. N_ν is related to the primordial abundance of ^{4}He by[33]

$$Y_P = 0.230 + 0.011 \ln 10^5 \eta + 0.013(N_\nu - 3) + 0.014(\tau_n - 10.6) , \tag{8.8}$$

where Y_P is the fraction of the mass of the Universe that is ^{4}He, η is the ratio of nucleons to photons, and τ_n is the neutron half-life in minutes.

Various limits on N_ν have been recently published.[34,35] These vary from

$$N_\nu < 5\text{–}6$$

to

$$N_\nu < 4 .$$

These limits cannot be assigned a confidence level because the uncertainties are systematic rather than statistical.

D. Summary of the lower limits set on the masses of SUSY particles from single-photon searches in e^+e^- experiments

The ASP, MAC, CELLO, and Mark J single-photon experiments have been interpreted to set lower limits on the masses of SUSY particles. We have combined the limits from these four experiments to form the best limits on the production of SUSY particles, using Eqs. (8.2) and (8.4) with $N = 3.86$ and $b = 6.0$. [We have used $N = 0$ and $b = 0.4$ for Mark J (Ref. 36).] The 90%-C.L. upper limit on n_{SUSY} is $n_{\text{SUSY}} < 4.0$. These results are summarized in Table V.

TABLE V. Summary of the lower limits set on SUSY masses from single-photon searches (GeV/c^2).

	CL	ASP	MAC (Ref. 28)	CELLO (Ref. 29)	Mark J (Ref. 37)	Combined
$m_{\tilde{e}}$ (degenerate)	90%	57	47	51.5	40	69
($m_{\tilde{\gamma}} = 0$)	95%	53		47.5	36	65
$m_{\tilde{e}}$ (nondegenerate)	90%	47	38	28		57
($m_{\tilde{\gamma}} = 0$)	95%	43		24		53
$m_{\tilde{W}}$	90%	59	48	40	45	73
($m_{\tilde{\nu}} = 0$)	95%	56		37	39	68

E. Non-single-photon limits on SUSY masses from e^+e^- collider experiments

There have been searches for processes other than the single-photon channel that have also set limits on these masses, all of which are consistent with the single-photon limits. The collaborations HRS (Ref. 11), CELLO (Ref. 38), JADE (Ref. 12), MAC (Ref. 39), Mark J (Ref. 40), and TASSO (Ref. 41) have attempted to detect the process $e^+e^-\to\tilde{e}^+\tilde{e}^-$ which is followed by the rapid decay $\tilde{e}\to\tilde{\gamma}e$. The signature is an acoplanar pair of electrons with missing energy. The absence of an anomalous rate for this signature gives the limit[12] $m_{\tilde{e}}>22$ GeV/c^2 (95% C.L.), assuming degenerate mass states and massless photino. Similar searches have also set limits on the masses of the supersymmetric partners of the muon[38,40,42] and the τ:[40,43] $m_{\tilde{\mu}}>21$ GeV/c^2 and $m_{\tilde{\tau}}>17$ GeV/c^2 (both 95% C.L.).

Several searches have also been made for events containing only a single electron detected in the final state. These events arise from $e^+e^-\to(e)\tilde{e}\tilde{\gamma}$, where the first outgoing electron does not leave the beam pipe, and the scalar electron decays as above. JADE (Ref. 12), MAC (Ref. 44), and Mark II (Ref. 45) have not observed any anomalous signal. The best limit is $m_{\tilde{e}}>30$ GeV/c^2 (95% C.L.) for degenerate mass states and massless photino.

A region in the $m_{\tilde{e}}$-$m_{\tilde{\gamma}}$ plane not addressed by ASP is $m_{\tilde{e}}<m_{\tilde{\gamma}}$. If the scalar electron is the LSP, then the signature for $e^+e^-\to\tilde{e}^+\tilde{e}^-$ will be a pair of charged particles. The best limit[12] obtained from a search for such events is $m_{\tilde{e}}>22$ GeV/c^2 (95% C.L.), for degenerate scalar electrons and $m_{\tilde{\gamma}}>m_{\tilde{e}}$.

The non-single-photon searches for W-ino production are very similar to those for scalar-electron production, and have been undertaken by JADE (Ref. 46), MAC (Ref. 44), and Mark (Ref. 47). The processes involved are $e^+e^-\to\tilde{W}^+\tilde{W}^-$ or $e^+e^-\to(e)\tilde{W}\tilde{\nu}$, in both cases followed by the rapid decay of the W-ino. MAC has assumed that the dominant decay is $\tilde{W}\to l\tilde{\nu}$, where l is a charged lepton, while JADE and Mark J have allowed additional modes. No signal has been observed and the W-ino mass has been limited[47] to $m_{\tilde{W}}>25$ GeV/c^2 (95% C.L.), for $m_{\tilde{\nu}}=0$. However, the approximations used in determining this limit have recently been questioned[44] and the limit has not yet been recalculated with the exact cross section.

These non-single-photon experiments have set less stringent limits on the masses of SUSY particles than the single-photon searches.

IX. CONCLUSION

There is no evidence for the existence of more than the known three generations of neutrinos. The current limits on N_ν are summarized in Fig. 23. This set of measurements, obtained using a variety of techniques, would appear to rule out any value for N_ν greater than five or possibly six.

The present single-photon measurement has increased the previous lower limit on SUSY-particle masses. No evidence has yet been observed for the existence of SUSY particles.

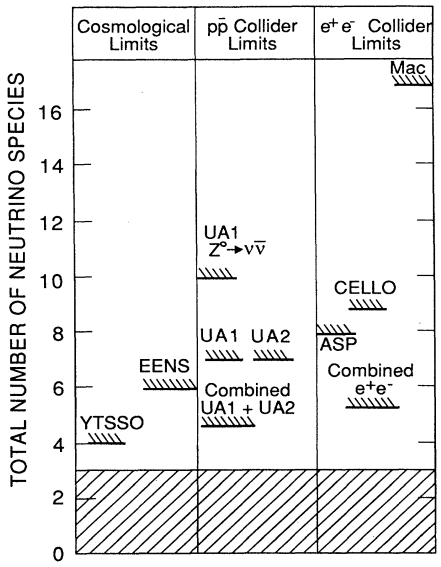

FIG. 23. Summary of limits on the number of generations of neutrinos.

ACKNOWLEDGMENTS

We thank D. Chambers, R. Baggs, D. Forbush, T. Lyons, C. Noyer, K. Scarpass, R. Stickley, F. Toevs, and other members of the Stanford Linear Accelerator Center, the Massachusetts Institute of Technology, Boston University, and the University of Washington for considerable technical assistance with the construction and installation of the detector. We are also grateful to the PEP operations staff. This work was supported in part by Department of Energy Contract Nos. DE-AC03-76SF00515, DE-AC02-86ER40284, and DE-AC02-76ER03071, and by National Science Foundation Grant No. PHY-8503215.

APPENDIX: CONTRIBUTIONS TO THE SINGLE-PHOTON CROSS SECTION FROM SUSY PARTICLES

The other particle that is frequently proposed as the LSP is the scalar neutrino ($\tilde{\nu}$), the SUSY partner of the neutrino.[48,49] The scalar neutrino interacts with ordinary matter via the weak force only, mediated either by the known $W^\pm$ and Z^0 or by their SUSY counterparts, the W-ino ($\tilde{W}$) or the Z-ino ($\tilde{Z}$). In general, the chargino mass states are mixtures of W-inos and Higgsinos. The model considered here, however, suggests that the W-ino is a mass eigenstate and is light compared to the other charginos. The masses of these SUSY gauge fermions are experimentally known to be at least comparable to that of their partners, so the scalar-neutrino interaction cross sections are of the same magnitude as those of the neutrinos. The processes that contribute to the single-photon rate are shown in Fig. 24. The unknown parameters in

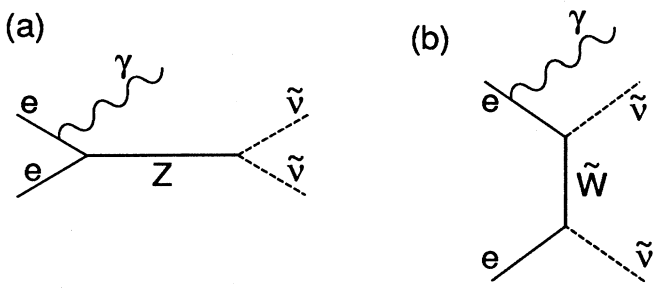

FIG. 24. Neutral-current (a) and charged-current (b) contributions to the radiative scalar-neutrino cross section. The charged current produces only electron-type scalar neutrinos, while the neutral current produces all types.

the scalar-neutrino cross section are the W-ino mass, N_ν, and the mass of each scalar-neutrino flavor. For the purposes of extracting limits on scalar-neutrino production, we make the simplifying assumption that $N_\nu=3$ and that the scalar-neutrino flavors are degenerate in mass. With these assumptions, the radiative scalar-neutrino cross section has the form of Eq. (2.4) in the local limit approximation, with[48]

$$\sigma_0=\sigma_{\tilde{\nu}\bar{\nu}} = \frac{G_F^2 s'}{12\pi}\left[\frac{\frac{1}{2}N_\nu(g_V^2+g_A^2)-\frac{1}{2}(g_V+g_A)m_W^4/m_{\tilde{W}}^4}{(1-s'/m_Z^2)^2+\Gamma_Z^2/m_Z^2} + \frac{1}{4}\frac{m_W^4}{m_{\tilde{W}}^4}\right](1-4m_{\tilde{\nu}}^2/s')^{3/2} . \quad \text{(A1)}$$

The structure of this equation is very similar to that of Eq. (2.2); the term in the large parentheses proportional to N_ν is due to the weak neutral-current production of all scalar-neutrino flavors, while the remaining terms in the large parentheses are due to the charged-current production of the electron scalar neutrino and interference terms. Because of spin factors, the cross section for the neutral-current production of each scalar-neutrino generation is only half of that of the corresponding neutrino generation;[50] hence the factor of $\frac{1}{2}$ multiplying N_ν. The exact α^3 cross section,[49] which was used to obtain limits, is shown as a function of the W-ino mass in Fig. 25. For $N_\nu=3$, $m_{\tilde{\nu}}=0$ and $m_{\tilde{W}}\leq 55$ GeV, ASP would expect to observe a single-photon signal inconsistent with $N_\nu=3$ at the 90% level (i.e., ≥ 4.5 events).

The radiative production of both the photino and the scalar neutrino would be a contribution to (1.1) regardless of which is the LSP. If the photino is the LSP, the scalar

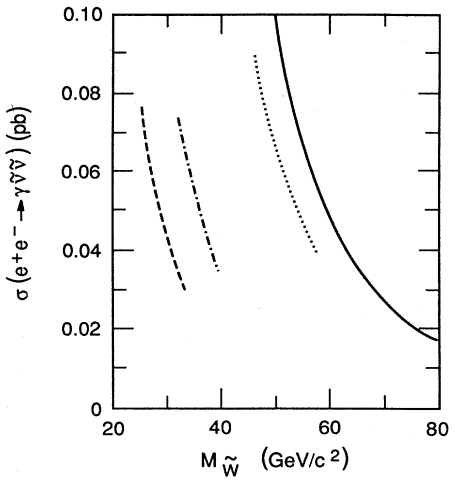

FIG. 25. The radiative scalar-neutrino cross section as a function of W-ino mass, for $m_{\tilde{\nu}}=0$ (solid), $m_{\tilde{\nu}}=6$ GeV (dotted), $m_{\tilde{\nu}}=11$ GeV (dashed-dotted), and $m_{\tilde{\nu}}=12$ GeV (dashed). The calculation assumes $N_\nu=3$.

neutrino will decay almost entirely by the mode $\tilde{\nu}\to\nu\tilde{\gamma}$. Conversely, if the scalar neutrino is LSP, the primary photino decay will be $\tilde{\gamma}\to\bar{\nu}\nu$. In either case, the decay products are noninteracting, so the SUSY contribution to the single-photon rate could actually be a sum of two different sources. For the purposes of extracting limits on SUSY masses, we assume that only one or the other is present; this is equivalent to assuming that $m_{\tilde{\nu}}$ (or $m_{\tilde{\gamma}})>\sqrt{s}/2$.

Other candidates for the lightest SUSY particle are the Higgsino ($\tilde{H}^0$) and the gravitino ($\tilde{G}$). The Higgsino has been largely ruled out as LSP by searches at DESY PETRA for events with two photons and large missing energy in the final state.[51] In any case, the Higgsino contribution to the single-photon rate is less than that of a single neutrino generation;[52] it will not be large enough to be detected by this experiment. If the gravitino is the LSP, the process contributing to the single-photon rate is $e^+e^-\to\gamma\tilde{\gamma}\tilde{G}$. The cross section is[53]

$$\sigma_{\gamma\tilde{\gamma}\tilde{G}}\approx\frac{m_{\tilde{e}}^4}{2\pi\alpha d^2}\sigma_{\gamma\tilde{\gamma}\tilde{\gamma}} . \quad \text{(A2)}$$

The SUSY scale-breaking term, $\sqrt{d}$, is expected[54] to be $\gtrsim 10^5$ GeV, so that the above coefficient is $\sim 10^{-12}$. This value of $\sqrt{d}$ also indicates that the photino is long lived,[53] so $e^+e^-\to\gamma\tilde{\gamma}\tilde{\gamma}$ will be the major SUSY contribution to the single-photon rate even if the gravitino is LSP.

---

*Present address: Lawrence Berkeley Laboratory, Berkeley, CA 94720.
†Permanent address: University of Geneva, Geneva, Switzerland.
‡Permanent address: Fermi National Accelerator Laboratory, Batavia, IL 60510.
§Present address: CERN, EP Division, CH-1211.

[1]ASP Collaboration, G. Bartha *et al.*, Phys. Rev. Lett. **56**, 685 (1986); ASP Collaboration, Hearty *et al.*, *ibid.* **58**, 1711 (1987). The limits for the number of neutrino species and the masses of the SUSY particles reported in these publications have been updated for this paper. To reduce the systematic error in our measurement of the integrated luminosity of this experiment, we have refined the analysis. The corrected luminosity is 5% lower than the previously reported luminosity of 115 pb^{-1}.

[2]S. Weinberg, Phys. Rev. Lett. **19**, 1264 (1967); A. Salam, in *Elementary Particle Theory; Relativistic Groups and Analyticity (Nobel Symposium No. 8)*, edited by N. Svartholm (Almqvist and Wiksell, Stockholm, 1968), p. 367; S. L. Glashow, J. Iliopoulos, and L. Maiani, Phys. Rev. D **2**, 1285 (1970). For a review of the standard model and references to the original literature, see C. Quigg, *Gauge Theories of the Strong, Weak, and Electromagnetic Interactions* (Benjamin/Cummings, Menlo Park, CA, 1983); I. J. R. Aitchison and A. J. G. Hey, *Gauge Theories in Particle Physics* (Hilger, Bristol, 1982).

[3]P. Fayet, Phys. Lett. **117B**, 460 (1982).

[4]J. Ellis and J. S. Hagelin, Phys. Lett. **122B**, 303 (1983).

[5]For recent reviews of supersymmetry, see H. E. Haber and G. L. Kane, Phys. Rep. **117**, 75 (1985); in *Supersymmetry*, proceedings of the Thirteenth SLAC Summer Institute on Particle Physics, Stanford, California, 1985, edited by E. C. Brennan (Stanford Linear Accelerator Center, Stanford, CA, 1986).

[6]K. J. F. Gaemers, R. Gastmans, and F. M. Renard, Phys. Rev. D **19**, 1605 (1979).

[7]L. Bento, J. C. Romão, and A. Barroso, Phys. Rev. D **33**, 1498 (1986).

[8]E. Ma and J. Okada, Phys. Rev. Lett. **41**, 287 (1978).

[9]G. Bonneau and F. Martin, Nucl. Phys. **B27**, 381 (1971).

[10]J. Ellis *et al.*, Nucl. Phys. **B238**, 453 (1984).

[11]HRS Collaboration, D. Bender *et al.*, Phys. Rev. D **30**, 515 (1983); R. J. Wilson, Report No. DOE/ER/01428-503-mc (microfiche), 1983, Purdue University, Ph.D. thesis.

[12]JADE Collaboration, W. Bartel *et al.*, Phys. Lett. **152B**, 385 (1985).

[13]K. Grassie and P. N. Pandita, Phys. Rev. D **30**, 22 (1984).

[14]D. Karlen, Nucl. Phys. **B289**, 23 (1987).

[15]ASP Collaboration, G. Bartha *et al.*, Nucl. Instrum. Methods (to be published).

[16]A later analysis improved the lead-glass-counter energy resolution to $\sigma_E/E = 10\%/\sqrt{E}$. See Ref. 15.

[17]The Z resolution varied from being the best in the center to being the worst at the ends. The average resolution was 1.5%. The major degradation to the resolution came from the electronic noise which accompanied the beam crossing. Bench tests of the central tracker obtained a Z resolution of 0.5%. The CT was strung with Stablohm 800 resistive wire which is available from California Fine Wire Company, Grover City, CA.

[18]R. J. Wilson, in *Proceedings of the Workshop on Triggering, Data Acquisition and Computing for High Energy/High Luminosity Hadron-Hadron Colliders*, Batavia, Illinois, 1986, edited by B. Cox, R. Fenner, and P. Hale (Fermilab, Batavia, IL, 1986), p. 118.

[19]M. Breidenbach, E. Frank, J. Hall, and D. Nelson, IEEE Trans. Nucl. Sci. **NS-25**, 706 (1978).

[20]A. G. Frodesen, O. Skjeggestad, and H. Tofte, *Probability and Statistics in Particle Physics* (Universitetsforlaget, Bergen, Norway, 1979).

[21]The differences between the classical and Bayesian approaches, and the advantages and disadvantages of each are discussed in W. T. Eadie *et al.*, *Statistical Methods in Experimental Physics* (Elsevier, New York, 1971), Sec. 2.2.5; H. B. Prosper, Nucl. Instrum. Methods **A241**, 236 (1985); V. L. Highland, Temple Report No. C00-3539-38, 1986 (unpublished).

[22]T. L. Lavine, Ph.D. thesis, University of Wisconsin, Report No. WISC-EX-86-275, 1986.

[23]J. F. Grivaz, in *The Standard Model: Supernova 1987A*, proceedings of the XXIInd Rencontres de Moriond, Les Arcs, France, 1987, edited by J. Tran Thanh Van (Editions Frontières, Gif-sur-Yvette, 1987), p. 115.

[24]F. A. Berends, G. J. H. Burgers, and W. L. Neerven, Phys. Lett. B **177**, 191 (1986).

[25]M. Igarashi and N. Nakazawa, Nucl. Phys. **B288**, 301 (1987).

[26]M. Bohm and T. Sack, Z. Phys. C **35**, 119 (1987).

[27]C. Mana, M. Martinez, and F. Cornet, DESY Report No. 86-114, 1986 (unpublished).

[28]MAC Collaboration, W. T. Ford *et al.*, Phys. Rev. D **33**, 3472 (1986). An erratum (unpublished) will correct the limits on SUSY masses in this paper to the values in T. Lavine's thesis (Ref. 22).

[29]CELLO Collaboration, H. J. Behrend *et al.*, Phys. Lett. B **215**, 186 (1988). The mass limits on $m_{\tilde{\omega}}$ and for the $m_{\tilde{e}}$ nondegenerate case are from H. J. Behrend *et al.*, *ibid.* **176**, 247 (1986).

[30]UA1 Collaboration, C. Albajar *et al.*, Phys. Lett. B **185**, 241 (1987).

[31]UA1 Collaboration, C. Albajar *et al.*, Phys. Lett. B **198**, 271 (1987).

[32]UA2 Collaboration, R. Ansari *et al.*, Phys. Lett. B **186**, 440 (1987).

[33]A. Boesgaard and G. Steigman, Annu. Rev. Astron. Astrophys. **23**, 319 (1985); J. Yang, M. S. Turner, G. Steigman, D. N. Schramm, and K. A. Olive, Astrophys. J. **281**, 493 (1984).

[34]J. Ellis, K. Enqvist, D. V. Nanopoulos, and S. Sarkar, Phys. Lett. **167B**, 457 (1986).

[35]G. Steigman, K. A. Olive, D. N. Schramm, and M. S. Turner, Phys. Lett. B **176**, 33 (1986).

[36]H. Wu, Ph.D. thesis, University of Hamburg, 1986.

[37]Mark J Collaboration, B. Adeva *et al.*, Phys. Lett. B **194**, 167 (1987).

[38]CELLO Collaboration, H. J. Behrend *et al.*, Phys. Lett. **144B**, 287 (1982).

[39]MAC Collaboration, E. Fernandez *et al.*, Phys. Rev. D **28**, 2721 (1983).

[40]Mark J Collaboration, B. Adeva *et al.*, Phys. Lett. **152B**, 439 (1985); Phys. Rep. **109**, 131 (1984).

[41]TASSO Collaboration, R. Brandelik *et al.*, Phys. Lett. **117B**, 365 (1982).

[42]JADE Collaboration, W. Bartel *et al.*, Phys. Lett. **152B**, 392 (1985).

[43]Mark II Collaboration, C. A. Blocker *et al.*, Phys. Rev. Lett. **49**, 517 (1982).

[44]MAC Collaboration, E. W. Fernandez *et al.*, Phys. Rev. D **35**, 374 (1987).

[45]Mark II Collaboration, L. Gladney *et al.*, Phys. Rev. Lett. **51**, 2253 (1983).

[46]JADE Collaboration, W. Bartel *et al.*, Z. Phys. C **29**, 505 (1985).

[47]Mark J Collaboration, B. Adeva *et al.*, Phys. Rev. Lett. **53**, 1806 (1984).

[48]J. S. Hagelin, G. L. Kane, and S. Raby, Nucl. Phys. **B241**, 638 (1984).

[49]J. A. Grifols, M. Martínez, and J. Solà, Nucl. Phys. **B268**, 151 (1986).

[50]R. M. Barnett, H. E. Haber, and K. S. Lackner, Phys. Lett. **126B**, 64 (1983).

[51]H. Komatsu and J. Kubo, Phys. Lett. **157B**, 90 (1985).

[52]H. E. Haber, in *Supersymmetry* (Ref. 5), p. 143.

[53]P. Fayet, Phys. Lett. B **175**, 471 (1986).

[54]J. Polchinski, in *Supersymmetry* (Ref. 5), p. 1.